


Article

In-Situ Construction of Fe-Doped NiOOH on the 3D Ni(OH)₂ Hierarchical Nanosheet Array for Efficient Electrocatalytic Oxygen Evolution Reaction

Mengyang Li ^{1,†}, Mingran Wang ^{1,†}, Qianwei Wang ¹, Yang Cao ¹, Jie Gao ¹, Zhicheng Wang ¹, Meiqi Gao ¹, Guosheng Duan ^{2,*} and Feng Cao ^{1,*} 

- ¹ Key Lab for Anisotropy and Texture of Materials (MoE), School of Materials Science and Engineering, Northeastern University, Shenyang 110819, China; 2310170@stu.neu.edu.cn (M.L.); 2200639@stu.neu.edu.cn (M.W.); 2270554@stu.neu.edu.cn (Q.W.); 2270359@stu.neu.edu.cn (Y.C.); 2300569@stu.neu.edu.cn (J.G.); 2300688@stu.neu.edu.cn (Z.W.); gaomq@smm.neu.edu.cn (M.G.)
- ² School of Safety Engineering, Shenyang Aerospace University, Shenyang 110136, China
- * Correspondence: duanguosheng@sau.edu.cn (G.D.); caof@atm.neu.edu.cn (F.C.)
- [†] These authors contributed equally to this work.

Abstract: Accessible and superior electrocatalysts to overcome the sluggish oxygen evolution reaction (OER) are pivotal for sustainable and low-cost hydrogen production through electrocatalytic water splitting. The iron and nickel oxohydroxide complexes are regarded as the most promising OER electrocatalyst attributed to their inexpensive costs, easy preparation, and robust stability. In particular, the Fe-doped NiOOH is widely deemed to be superior constituents for OER in an alkaline environment. However, the facile construction of robust Fe-doped NiOOH electrocatalysts is still a great challenge. Herein, we report the facile construction of Fe-doped NiOOH on Ni(OH)₂ hierarchical nanosheet arrays grown on nickel foam (FeNi@NiA) as efficient OER electrocatalysts through a facile in-situ electrochemical activation of FeNi-based Prussian blue analogues (PBA) derived from Ni(OH)₂. The resultant FeNi@NiA heterostructure shows high intrinsic activity for OER due to the modulation of the overall electronic energy state and the electrical conductivity. Importantly, the electrochemical measurement revealed that FeNi@NiA exhibits a low overpotential of 240 mV at 10 mA/cm² with a small Tafel slope of 62 mV dec⁻¹ in 1.0 M KOH, outperforming the commercial RuO₂ electrocatalysts for OER.

Keywords: OER activity; Fe-doped NiOOH; heterostructure; water-splitting; electrocatalysts



Citation: Li, M.; Wang, M.; Wang, Q.; Cao, Y.; Gao, J.; Wang, Z.; Gao, M.; Duan, G.; Cao, F. In-Situ Construction of Fe-Doped NiOOH on the 3D Ni(OH)₂ Hierarchical Nanosheet Array for Efficient Electrocatalytic Oxygen Evolution Reaction. *Materials* **2024**, *17*, 4670. <https://doi.org/10.3390/ma17184670>

Received: 2 August 2024

Revised: 20 September 2024

Accepted: 22 September 2024

Published: 23 September 2024



Copyright: © 2024 by the authors. Licensee MDPI, Basel, Switzerland. This article is an open access article distributed under the terms and conditions of the Creative Commons Attribution (CC BY) license (<https://creativecommons.org/licenses/by/4.0/>).

1. Introduction

The electrochemical decomposition of water is of considerable importance for the conversion and storage of renewable fuel cells and substitutable energy sources such as hydrogen, overcoming the difficulties of the depletion of non-renewable energy and serious environmental pollution [1–3]. Nonetheless, the oxygen evolution reaction (OER), an important half-cell reaction during water splitting, is severely restricted by its sluggish kinetic process [2,4]. Consequently, it is imperative to develop effective electrocatalysts that can expedite the reaction process and improve overall efficiency. Rare metal-derived materials, such as RuO₂ and IrO₂, are deemed the cutting-edge electrocatalysts for OER [5]. Despite their benefits, their industrial implementation is obstructed by the disadvantages of rarity, expensiveness, and deficient durability [6,7]. Hence, much effort has been put into the exploration of earth-abundant transition metal elements for developing catalysts with superior activity and endurance.

Transition metal-based oxides and hydroxides are extensively investigated as OER electrocatalysts attributed to their economic viability, high abundance, and unique 3D electronic structures [8,9]. Notably, Fe- and Ni-based hydroxides are widely deemed to

be identified as the foremost option for OER catalysis in alkaline media. For instance, various Fe/Ni-based oxides and hydroxides with distinct morphological, structural, and compositional attributes have been developed to improve OER activities [10–12]. Among them, the corresponding oxyhydroxides produced from surface reconstruction during OER were deemed to be one of the most active species under alkaline conditions [13–23]. Moreover, the optimized electronic structure and coordination sphere around Ni atoms by Fe-doping can expedite the rate of electron transfer and decrease the kinetic barrier. Hence, the Fe-doping can further enhance the intrinsic activity of Ni (oxy)hydroxides by about 30 and 1000 times [15,19,24–28].

Ni foam can be used as a substrate to fabricate Ni(OH)₂ hierarchical structures in situ for catalysis applications as a result of its excellent electrical conductivity and high porosity [29–35]. For instance, Kou et al. presented an accessible hydrothermal technique to modify Ni foam by applying Fe-doped β-Ni(OH)₂ nanosheets for boosting OER performance [36]. Nevertheless, a universal and fast approach to construct Fe-doped NiOOH for the efficient controlling of the surface reconstruction to achieve enhanced electrocatalysis for OER is rarely reported [37–40]. Previous studies have shown that FeNi PBA with a high surface area and uniform porosity can be reconstructed as Fe-doped NiOOH for enhanced oxygen evolution catalysis by cyclic voltammetry conditioning [41,42]. Nevertheless, PBA-derived catalysts exhibit low electrocatalytic activity and stability because of the poor conductivity of powder and mechanical loss [43–45]. Thus, a deeper in situ electrochemical activation to form Fe-doped NiOOH on 3D FeNi PBA as an open framework would be expected to be as effective and robust OER electrocatalysts.

In this work, FeNi-based PBA nanocubes were prepared via treating Ni(OH)₂ nanoarrays established on nickel foam through a mild ion exchange reaction. The OER electrocatalytic properties of Fe-doped NiOOH@Ni(OH)₂ were further enhanced by the electrochemical activating of the FeNi-PBA@Ni(OH)₂/Ni precursor. The incorporation of Fe is expected to modify the electronic structures and coordination environment of active atoms, promote the formation of Fe-doped NiOOH@Ni(OH)₂ heterostructures, and then improve the electron transfer rate by decreasing the kinetic barrier, thereby enhancing the OER performance. This well-designed composite exhibits a prominent performance for OER with a minimal overpotential of 240 mV at the current density of 10 mA/cm² and an ultralow Tafel slope of 62 mV dec^{−1}, which outperform recently reported catalysts, even RuO₂. This work adopts an electrochemical activation strategy, which proposes a new approach to the mechanism of reconstructing PBA or PBA derivatives on metal hydroxide substrates to synthesize metal-doped (oxy)hydroxide heterostructures.

2. Materials and Methods

2.1. Materials

The reagents Nickel nitrate hexahydrate (Ni(NO₃)₂·6H₂O), potassium ferricyanide (K₃[Fe(CN)₆]), urea, ammonium fluoride (NH₄F), nickel foam (NF), ruthenium dioxide (RuO₂), and Nafion (5 wt%) were all purchased from Sinopharm Group.

2.2. Preparation of Ni(OH)₂/Ni

Ni(NO₃)₂·6H₂O (0.131 g), urea (0.225 g), and NH₄F (0.056 g) were mixed in 150 mL of water and stirred with a magnetic stirrer until fully dissolved. The size of Ni foam was 1.5 cm × 4 cm with a thickness of 1.5 mm. It was cleaned by acetone and ethanol under ultrasonication conditions for 10 min, respectively, and then rinsed repeatedly with ethanol and water. The nickel foam was placed into the solution in a 100 mL Teflon-lined autoclave and heated at 120 °C in a drying oven for 2 h. The prepared sample was named Ni(OH)₂/NF.

2.3. Preparation of FeNi-PBA@Ni(OH)₂/Ni

Add 0.033 g of K₃[Fe(CN)₆] to 20 mL of water and stir magnetically until the substance is completely dissolved. The nickel foam with Ni(OH)₂ nanosheets was soaked in the

solution and left at room temperature for 24 h. The nickel foam was carefully removed after the process and rinsed thoroughly with deionized water and absolute ethanol. The prepared samples were named FeNi-PBA@Ni(OH)₂/Ni.

2.4. Preparation of FeNi@NiA

The FeNi-PBA@Ni(OH)₂/Ni was electrochemically stimulated in a three-electrode cell, where a carbon rod acted as the counter electrode, mercury oxide was the reference electrode, and the FeNi-PBA@Ni(OH)₂/Ni composite served as the working electrode. It was electrochemically activated at a constant potential of 0.65 V for 60 min. The prepared sample was named Fe-doped NiOOH@Ni(OH)₂ (FeNi@NiA).

2.5. Electrochemical Characterizations

Electrochemical measurements are performed with a Zennium E electrochemistry workstation (Zahner, Germany) in a standard three-electrode system. Detailed steps can be found in the Supplementary Information (SI).

2.6. Structural Characterization

The phase compositions of the catalysts were characterized by X-ray diffraction (XRD) on a Rigaku Smartlab diffractometer with CuKα irradiation. The surface was examined through scanning electron microscopy (SEM) on a JEOL JSM-7001F system and energy dispersive spectroscopy (EDS) mapping was examined at a voltage of 15 kV. X-ray photoelectron spectroscopy (XPS) measurements were conducted on a Thermo Fisher scientific (Waltham, MA, USA) Escalab 250Xi; the C1s peak at 284.8 eV was taken as a reference. The microstructures, morphology, and element analysis were carried out by transmission electron microscopy (TEM) on a JEOL JEM-2001F electron microscope at an accelerating voltage of 200 kV.

3. Results and Discussion

The synthesis process of FeNi@NiA is shown in Figure 1a, which mainly includes three steps. First, Ni(OH)₂ was synthesized via a one-step hydrothermal strategy on Ni foam to serve as an Ni precursor for FeNi-PBA growth. A three-dimensional (3D) structure of Ni foam with open channels and superior electrical conductivity ensures the adequate contact of the electrodes and interfaces and accelerates the charge and gas transport. Then, the eNi(OH)₂/Ni array was soaked in K₃[Fe(CN)₆] solution via a gentle ion-exchange method to obtain the bimetallic Fe-Ni PBA nanocubes supported on Ni(OH)₂. At the boundary between solid and liquid phases, the released Ni²⁺ would coordinate with Fe(CN)₆³⁻ in situ, then OH⁻ and Fe(CN)₆³⁻ undergo an ion exchange, resulting in the formation of PBA nanocubes on the Ni(OH)₂ nanosheet platforms. Finally, the FeNi@NiA electrode was obtained via electrochemical activation at 0.65 V for 1 h. In the process, the PBAs were oxidatively dissolved and transformed into the Fe-doped NiOOH, producing the resultant FeNi@NiA heterostructure.

XRD was carried out to verify the formation process of FeNi@NiA, as shown in Figure 1b. The peaks located at 44.5, 51.8, and 76.4° are associated with the (111), (200), and (220) lattice planes of FCC Ni (JCPDS NO. 04-0850). And a series of typical diffraction peaks of the XRD pattern of the nickel foam after hydrothermal treatment are well-indexed to the facets of Ni(OH)₂ (JCPDS NO. 14-0117), illustrating the formation of Ni(OH)₂ on nickel foam. As the ion exchange time is extended in K₃[Fe(CN)₆], the new diffraction peaks at 17.3, 24.6, and 35.1° can be indexed well to the (200), (220), and (400) crystal facets of KNiFe(CN)₆ (JCPDS NO. 51-1897) (Figure S1). We noticed the diffraction peaks of FeNi-PBA become stronger with the prolongation of immersion time, indicating the growth of FeNi-PBA on the Ni(OH)₂/NF. Notably, the diffraction peaks of FeNi-PBA disappear in the local enlarged XRD pattern of FeNi@NiA after the electrochemical activation (Figure S2). It is shown that the crystal structure of PBAs has been changed after electrochemical activation. A distinctive diffraction peak for Ni(OH)₂ is observed in the product, when

contrasted with the pre-activated one. Nevertheless, the intensity of the diffraction peak after electrochemical activation is significantly reduced, indicating the poor crystallinity of $\text{Ni}(\text{OH})_2$ after activation.

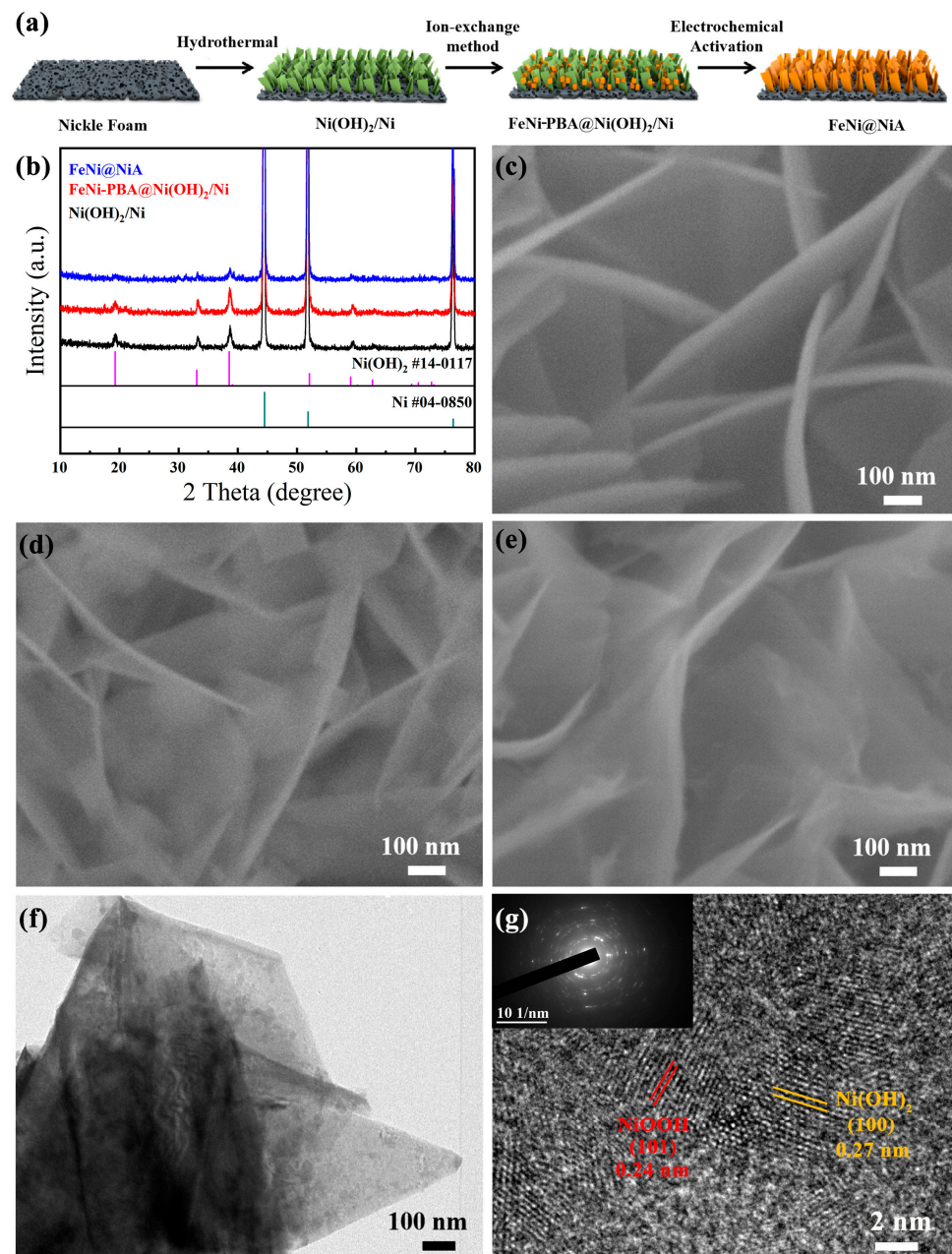


Figure 1. (a) Schematic illustration of the fabrication process of the hybrid; (b) XRD patterns before and after electrochemical activation; (c–e) SEM images of $\text{Ni}(\text{OH})_2/\text{Ni}$, $\text{FeNi-PBA@Ni}(\text{OH})_2/\text{Ni}$, and FeNi@NiA ; (f) TEM image of FeNi@NiA ; and (g) HRTEM image of FeNi@NiA (inset is the SAED pattern).

SEM was conducted to observe the morphological and structural evolution of the FeNi@NiA . As shown in Figure 1c, the $\text{Ni}(\text{OH})_2$ nanosheets are vertically aligned on Ni foam, showing a hierarchical array structure. The $\text{Ni}(\text{OH})_2$ nanosheets display a sleek, uniform surface and possess a thickness of roughly 30 nm. Such intercross and hierarchical nanosheet arrays on Ni foam are favorable for mass transfer and improving mechanical stability. The ion exchange gives rise to the FeNi-PBA nanocubes with dimensions of about 100 nm uniformly decorated on the $\text{Ni}(\text{OH})_2$ nanosheets (Figure 1c). Moreover,

with the prolongation of immersion time, closely packed PBA nanocubes were grown on the Ni(OH)₂ nanosheets (Figure S3). After the electrochemical activation in 1.0 M KOH, all the nanocubes on the Ni(OH)₂ nanosheets (FeNi-PBA@Ni(OH)₂/Ni) disappeared. The morphology of the nanosheets becomes irregular, indicating the in-situ formation of FeNi@NiA crumpled nanosheets with a larger geometric area to make contact more effectively with the electrolyte (Figure 1e).

TEM was performed to characterize the microstructure of the FeNi-PBA@Ni(OH)₂/Ni (Figure S4). The PBA nanocubes are uniformly distributed on the nanosheets. The average size of FeNi-PBA nanocubes is about 100 nm. Elemental mapping confirms the evenly dispersed of Ni, O, and N in the entire nanosheets, while Fe was selectively distributed in the corresponding nanocube regions (Figure S5). After CV conditioning, the FeNi@NiA exhibits nanosheet-like structures without nanocubes on the surfaces (Figure 1f). The interspacing of the measured inter-fringe distances are in agreement with the d-spacing of (101) crystal planes of NiOOH and (100) crystal planes of Ni(OH)₂, indicating the formation of heterostructures (Figure 1g) [36]. The elemental mapping analysis of FeNi@NiA by STEM measurement shows that the Fe, Ni, N, and O elements are homogeneously distributed on the nanosheets (Figure S6), confirming, indeed, the in-situ doping of Fe into the NiOOH@Ni(OH)₂. The selected-area electron diffraction (SAED) pattern of the Ni(OH)₂ nanosheet shows bright diffraction spots distributed in a regular hexagonal shape, indicating the single crystal structure exposed with a (001) facet (Figure S7) [37–39]. In the process of the in-situ ion exchange, nanocubes are gradually formed on nanosheets, in which monocrystals evolve into FeNi-PBA@Ni(OH)₂/Ni of the polycrystals as shown in Figure S8. After performing CV testing, the SAED pattern of FeNi@NiA still shows the ring features (Figure 1g, inset), suggesting the preserved polycrystalline structure. Through ion exchange and electrochemical activation, the structure was changed from single-crystal to polycrystalline, which greatly increases the electrochemically active area. Such a plentiful and staggered distribution of NiOOH and Ni(OH)₂ generates numerous interfaces and active sites, which can modulate the overall electronic energy state and thus enhance the catalytic activities [32].

The chemical composition and electronic configuration of FeNi-PBA@Ni(OH)₂/Ni and FeNi@NiA were further evaluated by XPS. For the Ni 2p of FeNi-PBA@Ni(OH)₂/Ni (Figure S9a), the Ni 2p XPS spectrum reveals two major peaks with binding energies at 873.7 and 856.1 eV, assigned to Ni 2p^{1/2} and Ni 2p^{3/2} [40,41]. The first doublet at 708.3 and 721.3 eV corresponds to the binding energies of Fe 2p^{3/2} and Fe 2p^{1/2} (Figure S9b), indicating the presence of Fe²⁺ in FeNi-PBA@Ni(OH)₂/Ni. The peaks observed at 712.3 and 724.3 eV are attributable to the presence of Fe³⁺ [42]. The O 1s spectrum shows two main peaks at 531.5 and 533.4 eV (Figure S9c), corresponding to the Ni-OH from the Ni(OH)₂ and adsorbed water species, respectively [42,43]. The peaks at 854.84 and 872.34 eV can be assigned to the Ni²⁺ of FeNi@NiA, while the peaks at 856.49 and 874.05 eV are related to the Ni³⁺ of the FeNi@NiA (Figure 2a), which provide solid evidence for the formation of NiOOH [44,45]. The first doublet at 708.3 and 721.9 eV corresponds to the binding energies of Fe 2p^{3/2} and Fe 2p^{1/2} (Figure 2b). The second one at 712.6 and 725.8 eV can be assigned to Fe³⁺, suggesting the binding energy of Fe is slightly positively shifted after electrochemical activation. For the O 1s spectrum, the peaks located at 531.5 and 533.4 eV are ascribed to the M-OH and the adsorbed water, respectively (Figure 2c). Moreover, the peaks at 530.5 eV are ascribed to the Ni-O-Ni bond in the O 1s spectrum of FeNi@NiA, which further prove the constitution of the NiOOH after electrochemical activation (Figure 2c) [42,45]. The above results indicate the successful construction of Fe-doping NiOOH/Ni(OH)₂ heterostructures, which will effectively regulate the electronic energy state of the active sites in catalytic reactions. This modulation impacts the Gibbs free energy and the dynamics of charge transfer, thereby promoting the catalyst's performance [46].

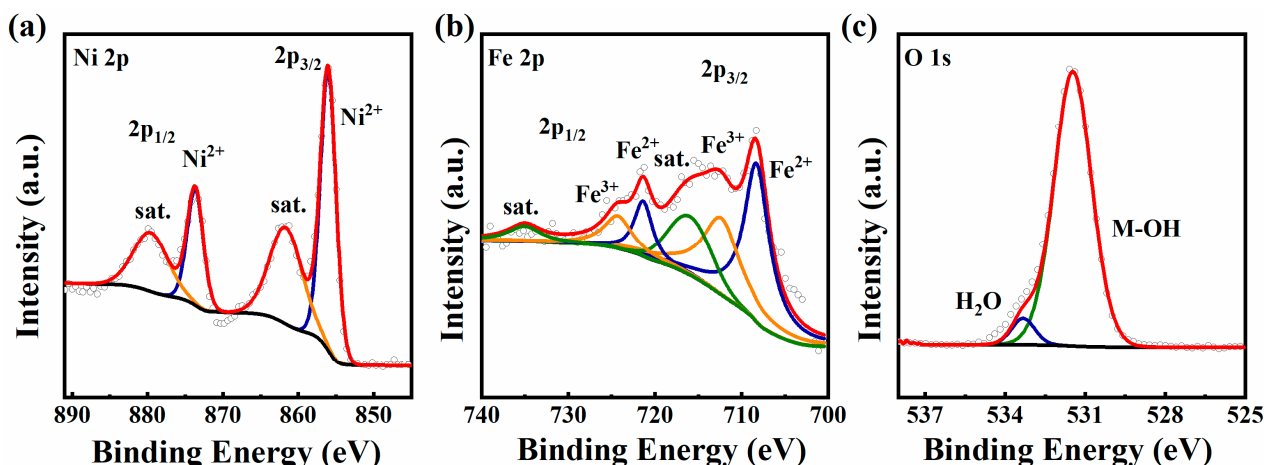


Figure 2. XPS spectra of FeNi@NiA: (a) Ni 2p; (b) Fe 2p; and (c) O 1s high-resolution XPS spectra.

The catalytic performances of the FeNi@NiA nanosheets for OER were investigated through linear sweep voltammetry conducted in an N_2 -saturated 1.0 M KOH in a three-electrode system. An iR compensation was implemented for all the initial electrochemical data. As shown in Figure 3a, linear sweep voltammetry (LSV) curves reveal that the FeNi@NiA electrode presents the lowest overpotential of 240 mV at a current density of 10 mA/cm², which is much smaller than those of FeNi-PBA@Ni(OH)₂/Ni (285 mV), FeNi-PBA/NiA (310 mV), FeNi-PBA/Ni (415 mV), Ni(OH)₂/Ni (358 mV), Ni(OH)₂/NiA (370 mV), and RuO₂ loaded on Ni foam (303 mV). The much lower overpotential of the FeNi@NiA indicates remarkable OER activity under alkaline conditions. To further assess the intrinsic catalytic activity, the kinetics of OER were evaluated through the corresponding Tafel plots (Figure 3b). The Tafel slope has been used to dissect the kinetics of the rate-determining step in the OER process. The Tafel slope of the FeNi@NiA is only 62.1 mV dec⁻¹, which is vastly superior to those of FeNi-PBA@Ni(OH)₂/Ni (70.4 mV dec⁻¹), FeNi-PBA/NiA (98.7 mV dec⁻¹), FeNi-PBA/Ni (115.9 mV dec⁻¹), Ni(OH)₂/NiA (179.9 mV dec⁻¹), Ni(OH)₂/Ni (86.6 mV dec⁻¹), and RuO₂ (76.6 mV dec⁻¹). The lowest Tafel slope of FeNi@NiA reveals the fastest OER kinetics and the easiest charge transfer process. Electrochemical impedance spectroscopy (EIS) analysis was performed on all the samples (Figure 3c). The FeNi@NiA shows the smallest charge-transfer resistance (R_{ct}), which is considerably smaller than all the other values, respectively. This indicates that faster electron transfer and ion transport occur at the FeNi@NiA interface. Additionally, the double-layer capacitance (C_{dl}), which is generally used to estimate the electrochemical surface area (ECSA), was measured to assess the catalytic performance of the FeNi@NiA electrode (Figure 3d). The FeNi@NiA electrode has the highest C_{dl} value (4.10 mF/cm²), which is much higher than that of NiFe-PBA@Ni(OH)₂/Ni and Ni(OH)₂/Ni, revealing that the construction of the Fe-NiOOH@Ni(OH)₂ heterojunction and the large specific surface area of Ni(OH)₂ nanosheets endow the material with more OER active sites and can provide more electron pathways. FeNi@NiA exhibited the largest ECSA value of 102.5 (Table S1), indicating the most exposed active sites, thus promoting increased activity. To evaluate the intrinsic activity of the specific active site, we normalized the OER current to the ECSA (j_{ECSA}) (Figure 3e). FeNi@NiA shows a j_{ECSA} of 10 mA/cm² at a low overpotential of 297 mV. At the same overpotential, NiFe-PBA@Ni(OH)₂/NF and Ni(OH)₂/NF, respectively, exhibit a much smaller j_{ECSA} of 4.42 and 1.36 mA/cm², and the bare Ni foam has the smallest j_{ECSA} of only 1.2 mA/cm². These results also indicate that the intrinsic activity of FeNi@NiA is much higher than that of FeNi-PBA@Ni(OH)₂/Ni and Ni(OH)₂/Ni [47].

The synergistic effect of the FeNi@NiA heterostructure not only increased the highly electrochemically active surface area but also can further facilitate its intrinsic activity for OER through modulating the overall electronic energy state. On this basis, the incorporation of Fe can promote the conductivity of NiOOH and optimize the adsorption energy of OER

intermediates [48,49]. Most significantly, the results also confirm that the outstanding OER activity of Fe-NiOOH@Ni(OH)₂ is also attributed to the increased ECSA and the enhanced intrinsic activity of each active site in converting OH⁻ into O₂. The FeNi@NiA demonstrates the most minimal overpotential of 240 mV at $j_{\text{geo}} = 10 \text{ mA/cm}^2$, which surpasses many other state-of-the-art OER electrocatalysts (Figure 3f) [47,50–60].

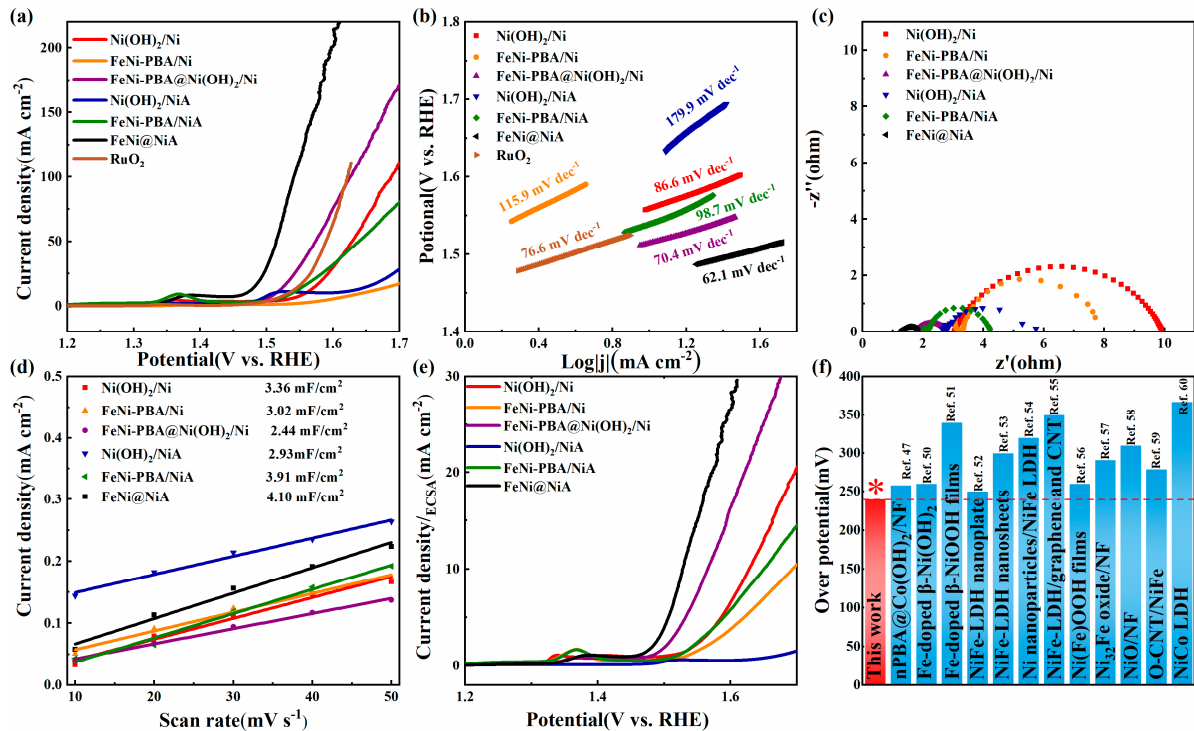


Figure 3. (a) The polarization curves at a scan rate of 5 mV/s (with iR correction) of various electrocatalysts for OER in 1.0 M KOH solution; (b) Tafel plots; (c) EIS spectrum (at a bias voltage of 1.5 V vs. RHE with the frequency range from 0.1 Hz to 100 K Hz) and (d) C_{dl} of various electrocatalysts determined from the CV curves measured across a spectrum of scan rates; (e) polarization curves with current density normalized to the ECSA; and (f) comparison of the overpotential of FeNi@NiA at 10 mA/cm² in this study with those of other catalysts documented in recent publications.

The stability of the catalyst is also vital to its commercial application. Long-term durability measurements were carried out by chronoamperometric and cyclic voltammetry in 1 M KOH of FeNi@NiA. The current density remained stable without significant degradation over 20 h (Figure 4a). The polarization curve exhibited minimal change in comparison to its initial state (Figure 4a, inset), indicating that the sample still maintains high OER activity and excellent durability due to the robust heterostructures. The oxyhydroxide and hydroxide can improve the durability of the electrocatalyst in a strong alkaline environment. After the electrochemical test, the collected sample shows similar XRD patterns as the initial sample, suggesting that the phase structure nearly does not change. The SEM and the TEM characterization also verify the well-retained microstructure of FeNi@NiA. The lattice finger of 0.27 nm in the HRTEM image can be still found and ascribed to the lattice plane (100) of Ni(OH)₂ (Figure S10), suggesting that the crystal structure of FeNi@NiA remains unchanged even after a long-term durability test.

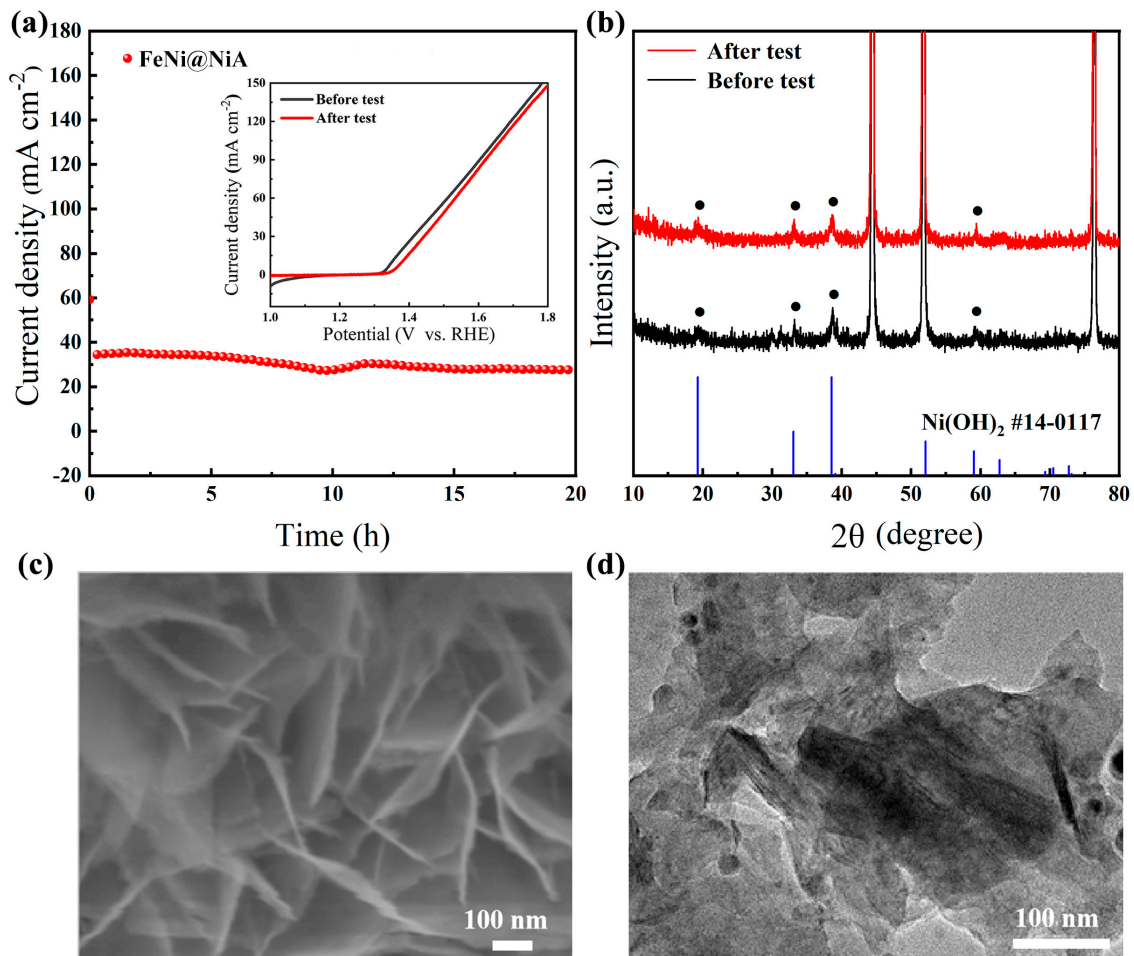


Figure 4. (a) The chronoamperometric measurement of FeNi@NiA for OER at an overpotential of 0.7 V (inset is the LSV curves of before and after durability test); (b) XRD pattern; (c) SEM image; and (d) TEM image of FeNi@NiA after durability test.

We further evaluated the overall water-splitting performance involved in assigning the FeNi@NiA electrode as the anode and the commercial Pt/C/Ni as the cathode in a two-electrode system. As shown in Figure 5a, the cell delivers a current density of 10 mA/cm² at a voltage of 1.55 V. This value is much lower than that of an electrolyzer constructed by an RuO₂/Ni anode and a Pt/C/Ni cathode (1.65 V). As a proof of demonstration, the electrolyzer can be driven using a 1.5 V commercial dry battery as the energy source (inset in Figure 5a). Notably, the performance at the current density of 10 mA/cm² also surpasses most non-noble metal catalysts for overall alkaline water splitting (Figure 5c) [61–73]. The cathode/anode exhibits steady rates of H₂ and O₂ evolution with a ratio of approximately 2:1, which matches well with the theoretical value during electrolysis and indicates an almost perfect 100% Faradaic efficiency (Figure 5b). This proves that FeNi@NiA is an efficient and durable electrocatalyst for overall water splitting. The durability test of FeNi@NiA shows a stable potential at 20 mA/cm² for over 55 h, both suggesting stability for water splitting (Figure 5d). The continuous generation of gas bubbles are visible on the electrode surfaces during the electrolysis process.

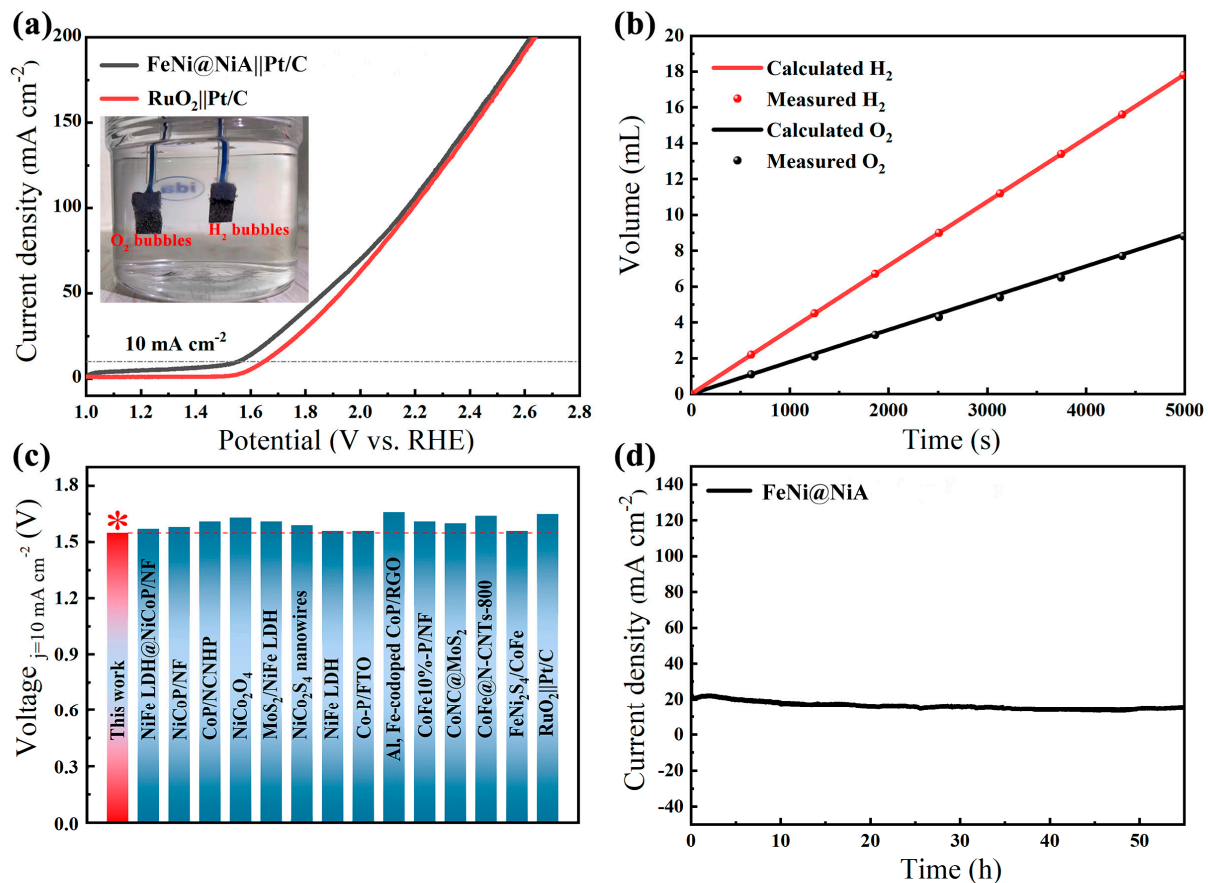


Figure 5. (a) LSV of the typical two-electrode system using FeNi@NiA as the anode and Pt/C/Ni as the cathode in 1.0 M KOH; commercial RuO₂/Ni||Pt/C/Ni was also tested for comparison (inset: photograph of the two-electrode device); (b) the volumes of H₂ and O₂ gases generated in relation to the duration of the water-splitting process; (c) the comparison of cell voltages for achieving a 10 mA cm⁻² for the FeNi@NiA with the performance of other OER catalysts from recent reports; and (d) time-dependent current density curve for FeNi@NiA in a two-electrode cell.

4. Conclusions

In summary, we achieved the in-situ construction of Fe-doped NiOOH on hierarchical Ni(OH)₂ nanosheet arrays as a flexible and precise treatment method on nickel foam acting as a state-of-the-art electrode. Electrochemical activation was applied to synthesize in-situ surface-activated FeNi@NiA self-supporting electrodes with the nanosheet structure from the templated NiFe-based PBA nanocubes. The formation of the FeNi@NiA heterojunction is demonstrated to be more thermodynamically favorable for OER in alkaline electrolytes, which exhibited an impressive overpotential of 240 mV to achieve a current density of 10 mA/cm². As explored for overall water splitting, the alkali-electrolyzer based on the FeNi@Ni achieves a current density of 10 mA/cm² with a minimal cell voltage of 1.55 V with outstanding durability over 55 h. This work opens up a new avenue for the reconstruction of Prussian blue analogues, while also presenting a straightforward approach to crafting potent, economical, and efficient OER electrocatalysts.

Supplementary Materials: The following supporting information can be downloaded at: <https://www.mdpi.com/article/10.3390/ma17184670/s1>, Figure S1: XRD pattern for FeNi-PBA@Ni(OH)₂/Ni with different immersion time of 0 h, 2 h, 12 h, 24 h, and 48 h; Figure S2: XRD pattern for FeNi@NiA and FeNi-PBA@Ni(OH)₂/Ni; Figure S3: SEM pattern for FeNi-PBA@Ni(OH)₂/Ni with different immersion time of 2 h, 12 h, 24 h, and 48 h; Figure S4: The low-resolution TEM images of FeNi-PBA@Ni(OH)₂/Ni; Figure S5: High-angle annular dark field-TEM image of FeNi-PBA@Ni(OH)₂/Ni and the corresponding elemental mapping images of Fe, Ni, N, and O; Figure S6: High-angle annular

dark field-TEM image of FeNi@NiA and the corresponding elemental mapping images of Fe, Ni, N, and O; Figure S7: SAED pattern of Ni(OH)₂/Ni; Figure S8: SAED pattern of FeNi-PBA@Ni(OH)₂/Ni; Figure S9: XPS of FeNi-PBA@Ni(OH)₂/Ni (a) Ni 2p, (b) Fe 2p, and (c) O 1s; Figure S10: HR-TEM image of FeNi@NiA after durability test; Table S1: The ECSA of the sample.

Author Contributions: M.L. and M.W.: methodology, experiment, validation, writing—original draft preparation, and writing—review and editing. Q.W., Y.C., J.G., Z.W. and M.G.: investigation, resources, and data curation. G.D. and F.C.: conceptualization, visualization, writing—review and editing, supervision, project administration, and funding acquisition. All authors have read and agreed to the published version of the manuscript.

Funding: This work was supported by the National Natural Science Foundation of China (52371150), and the Natural Science Foundation of Liaoning Province of China (2023-MS070).

Data Availability Statement: All data generated for this work are included in this article.

Acknowledgments: We gratefully acknowledge the financial aid provided by the National Natural Science Foundation of China, and the Natural Science Foundation of Liaoning Province of China.

Conflicts of Interest: The authors declare no conflicts of interest.

References

1. Gao, X.; Chen, Y.; Wang, Y.; Zhao, L.; Zhao, X.; Du, J.; Wu, H.; Chen, A. Next-Generation Green Hydrogen: Progress and Perspective from Electricity, Catalyst to Electrolyte in Electrocatalytic Water Splitting. *Nanomicro Lett.* **2024**, *16*, 237. [[CrossRef](#)] [[PubMed](#)]
2. Pan, G.; Gu, W.; Hu, Q.; Wang, J.; Teng, F.; Strbac, G. Cost and low-carbon competitiveness of electrolytic hydrogen in China. *Energy Environ. Sci.* **2021**, *14*, 4868–4881. [[CrossRef](#)]
3. Xia, G.; Habibullah; Xie, Q.; Huang, Q.; Ye, M.; Gong, B.; Du, R.; Wang, Y.; Yan, Y.; Chen, Y.; et al. Recent progress in carbonaceous materials for the hydrogen cycle: Electrolytic water splitting, hydrogen storage and fuel cells. *Chem. Eng. J.* **2024**, *495*, 153405. [[CrossRef](#)]
4. Zhu, J.; Hu, L.; Zhao, P.; Lee, L.Y.S.; Wong, K.Y. Recent Advances in Electrocatalytic Hydrogen Evolution Using Nanoparticles. *Chem. Rev.* **2020**, *120*, 851–918. [[CrossRef](#)]
5. Over, H. Fundamental Studies of Planar Single-Crystalline Oxide Model Electrodes (RuO₂, IrO₂) for Acidic Water Splitting. *ACS Catal.* **2021**, *11*, 8848–8871. [[CrossRef](#)]
6. Zhang, H.; Hagen, D.J.; Li, X.; Graff, A.; Heyroth, F.; Fuhrmann, B.; Kostanovskiy, I.; Schweizer, S.L.; Caddeo, F.; Maijenburg, A.W.; et al. Atomic Layer Deposition of Cobalt Phosphide for Efficient Water Splitting. *Chem. Int. Ed.* **2020**, *59*, 17172–17176. [[CrossRef](#)]
7. Zhao, D.; Zhuang, Z.; Cao, X.; Zhang, C.; Peng, Q.; Chen, C.; Li, Y. Atomic site electrocatalysts for water splitting, oxygen reduction and selective oxidation. *Chem. Soc. Rev.* **2020**, *49*, 2215–2264. [[CrossRef](#)]
8. Jeong, H.; Jang, H.; Kim, Y.H.; Kim, M.; Kang, Y.; Myung, J.h. Surface exsolved NiFeO_x nanocatalyst for enhanced alkaline oxygen evolution catalysis. *Appl. Surf. Sci.* **2024**, *662*, 160134. [[CrossRef](#)]
9. Liu, Y.; Jiang, Z.; Jiang, Z.-J. Plasma-Assisted Formation of Oxygen Defective NiCoO/NiCoN Heterostructure with Improved ORR/OER Activities for Highly Durable All-Solid-State Zinc-Air Batteries. *Adv. Funct. Mater.* **2023**, *33*, 2302883. [[CrossRef](#)]
10. Wang, Y.; Tao, S.; Lin, H.; Wang, G.; Zhao, K.; Cai, R.; Tao, K.; Zhang, C.; Sun, M.; Hu, J.; et al. Atomically targeting NiFe LDH to create multivacancies for OER catalysis with a small organic anchor. *Nano Energy* **2021**, *81*, 105606. [[CrossRef](#)]
11. Wan, C.; Jin, J.; Wei, X.; Chen, S.; Zhang, Y.; Zhu, T.; Qu, H. Inducing the SnO₂-based electron transport layer into NiFe LDH/NF as efficient catalyst for OER and methanol oxidation reaction. *J. Mater. Sci. Technol.* **2022**, *124*, 102–108. [[CrossRef](#)]
12. Gong, L.; Yang, H.; Douka, A.I.; Yan, Y.; Xia, B.Y. Recent Progress on NiFe-Based Electrocatalysts for Alkaline Oxygen Evolution. *Adv. Sustain. Syst.* **2021**, *5*, 2000136. [[CrossRef](#)]
13. Kim, B.-J.; Fabbri, E.; Abbott, D.F.; Cheng, X.; Clark, A.H.; Nachttegaal, M.; Borlaf, M.; Castelli, I.E.; Graule, T.; Schmidt, T.J. Functional Role of Fe-Doping in Co-Based Perovskite Oxide Catalysts for Oxygen Evolution Reaction. *J. Am. Chem. Soc.* **2019**, *141*, 5231–5240. [[CrossRef](#)]
14. Rajan, A.G.; Martirez, J.M.P.; Carter, E.A. Facet-Independent Oxygen Evolution Activity of Pure β-NiOOH: Different Chemistries Leading to Similar Overpotentials. *J. Am. Chem. Soc.* **2020**, *142*, 3600–3612. [[CrossRef](#)]
15. Mou, Q.; Xu, Z.; Zuo, W.; Shi, T.; Li, E.; Cheng, G.; Liu, X.; Zheng, H.; Li, H.; Zhao, P. Metal-organic-framework embellished through ion etching method for highly enhanced electrochemical oxygen evolution reaction catalysis. *Mater. Chem. Front.* **2022**, *6*, 2750–2759. [[CrossRef](#)]
16. Fabbri, E.; Nachttegaal, M.; Binninger, T.; Cheng, X.; Kim, B.-J.; Durst, J.; Bozza, F.; Graule, T.; Schaublin, R.; Wiles, L.; et al. Dynamic surface self-reconstruction is the key of highly active perovskite nano-electrocatalysts for water splitting. *Nat. Mater.* **2017**, *16*, 925–931. [[CrossRef](#)]

17. Zhao, Y.; Zhang, X.; Jia, X.; Waterhouse, G.I.N.; Shi, R.; Zhang, X.; Zhan, F.; Tao, Y.; Wu, L.Z.; Tung, C.-H.; et al. Sub-3 nm Ultrafine Monolayer Layered Double Hydroxide Nanosheets for Electrochemical Water Oxidation. *Adv. Energy Mater.* **2018**, *8*, 1703585. [[CrossRef](#)]
18. Tang, M.; He, Y.-M.; Ali, A.; Zhu, J.L.; Shen, P.K.; Ouyang, Y.-F. In-situ generate robust Fe-Ni derived nano-catalyst featuring surface reconstruction for enhanced oxygen evolution reaction. *Int. J. Hydrogen Energy* **2022**, *47*, 28303–28312. [[CrossRef](#)]
19. He, Z.-D.; Tesch, R.; Eslamibidgoli, M.J.; Eikerling, M.H.; Kowalski, P.M. Low-spin state of Fe in Fe-doped NiOOH electrocatalysts. *Nat. Commun.* **2023**, *14*, 3498. [[CrossRef](#)]
20. Zhong, H.; Wang, X.; Sun, G.; Tang, Y.; Tan, S.; He, Q.; Zhang, J.; Xiong, T.; Diao, C.; Yu, Z.; et al. Optimization of oxygen evolution activity by tuning e^*_g band broadening in nickel oxyhydroxide. *Energy Environ. Sci.* **2023**, *16*, 641–652. [[CrossRef](#)]
21. Guo, K.; Jia, J.; Lu, X.; Wang, S.; Wang, H.; Wu, H.; Xu, C. F-doped NiOOH derived from progressive reconstruction for efficient and durable water oxidation. *Inorg. Chem. Front.* **2024**, *11*, 1479–1491. [[CrossRef](#)]
22. Yin, Z.H.; Huang, Y.; Song, K.; Li, T.T.; Cui, J.-Y.; Meng, C.; Zhang, H.; Wang, J.J. Ir Single Atoms Boost Metal-Oxygen Covalency on Selenide-Derived NiOOH for Direct Intramolecular Oxygen Coupling. *J. Am. Chem. Soc.* **2024**, *146*, 6846–6855. [[CrossRef](#)] [[PubMed](#)]
23. Chen, R.; Yang, Y.; Wu, W.; Chen, S.; Wang, Z.; Zhu, Y.; Cheng, N. Reconstructed β -NiOOH enabling highly efficient and ultrastable oxygen evolution at large current density. *Chem. Eng. J.* **2024**, *480*, 148100. [[CrossRef](#)]
24. Shi, P.; Cheng, X.; Lyu, S. Efficient electrocatalytic oxygen evolution at ultra-high current densities over 3D Fe, N doped Ni(OH)₂ nanosheets. *Chin. Chem. Lett.* **2021**, *32*, 1210–1214. [[CrossRef](#)]
25. Peng, Y.; Hajiyani, H.; Pentcheva, R. Influence of Fe and Ni Doping on the OER Performance at the Co₃O₄(001) Surface: Insights from DFT+U Calculations. *ACS Catal.* **2021**, *11*, 5601–5613. [[CrossRef](#)]
26. Ye, Q.; Liu, J.; Lin, L.; Sun, M.; Wang, Y.; Cheng, Y. Fe and P dual-doped nickel carbonate hydroxide/carbon nanotube hybrid electrocatalysts for an efficient oxygen evolution reaction. *Nanoscale* **2022**, *14*, 6648–6655. [[CrossRef](#)]
27. Wei, Y.; Yi, L.; Wang, R.; Li, J.; Li, D.; Li, T.; Sun, W.; Hu, W. A Unique Etching-Doping Route to Fe/Mo Co-Doped Ni Oxyhydroxide Catalyst for Enhanced Oxygen Evolution Reaction. *Small* **2023**, *19*, 2301267. [[CrossRef](#)]
28. Trzesniewski, B.J.; Diaz-Morales, O.; Vermaas, D.A.; Longo, A.; Bras, W.; Koper, M.T.M.; Smith, W.A. In Situ Observation of Active Oxygen Species in Fe-Containing Ni-Based Oxygen Evolution Catalysts: The Effect of pH on Electrochemical Activity. *J. Am. Chem. Soc.* **2015**, *137*, 15112–15121. [[CrossRef](#)]
29. Browne, M.P.; Vasconcelos, J.M.; Coelho, J.; O'Brien, M.; Rovetta, A.A.; McCarthy, E.K.; Nolan, H.; Duesberg, G.S.; Nicolosi, V.; Colavita, P.E.; et al. Improving the performance of porous nickel foam for water oxidation using hydrothermally prepared Ni and Fe metal oxides. *Sustain. Energy Fuels* **2017**, *1*, 207–216. [[CrossRef](#)]
30. He, W.; Ren, G.; Li, Y.; Jia, D.; Li, S.; Cheng, J.; Liu, C.; Hao, Q.; Zhang, J.; Liu, H. Amorphous nickel-iron hydroxide films on nickel sulfide nanoparticles for the oxygen evolution reaction. *Catal. Sci. Technol.* **2020**, *10*, 1708–1713. [[CrossRef](#)]
31. Zhang, Y.; Ye, L.; Zhang, M.; Ma, L.; Gong, Y. A nanoflower composite catalyst in situ grown on conductive iron foam: Revealing the enhancement of OER activity by cooperating of amorphous Ni based nanosheets with spinel NiFe₂O₄. *Appl. Surf. Sci.* **2022**, *589*, 152957. [[CrossRef](#)]
32. Klaus, S.; Cai, Y.; Louie, M.W.; Trotochaud, L.; Bell, A.T. Effects of Fe Electrolyte Impurities on Ni(OH)₂/NiOOH Structure and Oxygen Evolution Activity. *J. Phys. Chem. C* **2015**, *119*, 7243–7254. [[CrossRef](#)]
33. Guo, Y.; Wang, P.; Li, P.; Tang, M.; Yin, H.; Wang, D. A highly efficient and durable self-standing iron-cobalt-nickel trimetallic phosphide electrode for oxygen evolution reaction. *J. Alloys Compd.* **2023**, *960*, 170493. [[CrossRef](#)]
34. Park, J.H.; Kwon, H.J.; Lee, D.Y.; Suh, S.J. Effect of Ni Sulfate Residue on Oxygen Evolution Reaction (OER) in Porous NiFe@NiFe Layered Double Hydroxide. *Small* **2024**, *20*, 2400046. [[CrossRef](#)]
35. He, L.; Cai, Z.; Zheng, D.; Ouyang, L.; He, X.; Chen, J.; Li, Y.; Guo, X.; Liu, Q.; Li, L.; et al. Three-dimensional porous NiCoP foam enabled high-performance overall seawater splitting at high current density. *J. Mater. Chem. A* **2024**, *12*, 2680–2684. [[CrossRef](#)]
36. Kou, T.; Wang, S.; Hauser, J.L.; Chen, M.; Oliver, S.R.J.; Ye, Y.; Guo, J.; Li, Y. Ni Foam-Supported Fe-Doped β -Ni(OH)₂ Nanosheets Show Ultralow Overpotential for Oxygen Evolution Reaction. *ACS Energy Lett.* **2019**, *4*, 622–628. [[CrossRef](#)]
37. Shukla, A.K.; Ercius, P.; Gautam, A.R.S.; Cabana, J.; Dahmen, U. Electron Tomography Analysis of Reaction Path during Formation of Nanoporous NiO by Solid State Decomposition. *Growth Des.* **2014**, *14*, 2453–2459. [[CrossRef](#)]
38. Gao, T.; Jelle, B.P. Paraotwayite-type α -Ni(OH)₂ Nanowires: Structural, Optical, and Electrochemical Properties. *J. Phys. Chem. C* **2013**, *117*, 17294–17302. [[CrossRef](#)]
39. Zhou, W.; Yao, M.; Guo, L.; Li, Y.; Li, J.; Yang, S. Hydrazine-Linked Convergent Self-Assembly of Sophisticated Concave Polyhedrons of β -Ni(OH)₂ and NiO from Nanoplate Building Blocks. *J. Am. Chem. Soc.* **2009**, *131*, 2959–2964. [[CrossRef](#)]
40. Feng, Y.; Han, H.; Kim, K.M.; Dutta, S.; Song, T. Self-templated Prussian blue analogue for efficient and robust electrochemical water oxidation. *J. Catal.* **2019**, *369*, 168–174. [[CrossRef](#)]
41. Zhang, X.; Khan, I.U.; Huo, S.; Zhao, Y.; Liang, B.; Li, K.; Wang, H. In-situ integration of nickel-iron Prussian blue analog heterostructure on Ni foam by chemical corrosion and partial conversion for oxygen evolution reaction. *Electrochim. Acta* **2020**, *363*, 137211. [[CrossRef](#)]
42. Xu, X.; Wang, T.; Su, L.; Zhang, Y.; Dong, L.; Miao, X. In Situ Synthesis of Superhydrophilic Amorphous NiFe Prussian Blue Analogues for the Oxygen Evolution Reaction at a High Current Density. *ACS Sustain. Chem. Eng.* **2021**, *9*, 5693–5704. [[CrossRef](#)]

43. Ma, F.; Wu, Q.; Liu, M.; Zheng, L.; Tong, F.; Wang, Z.; Wang, P.; Liu, Y.; Cheng, H.; Dai, Y.; et al. Surface Fluorination Engineering of NiFe Prussian Blue Analogue Derivatives for Highly Efficient Oxygen Evolution Reaction. *ACS Appl. Mater. Interfaces* **2021**, *13*, 5142–5152. [[CrossRef](#)] [[PubMed](#)]
44. Li, C.; Sun, F.; Qin, X.; Yang, K.; Wu, W. A general strategy for Ni⁰-NiOOH hybrid catalyst of high hydrogen evolution activity. *Int. J. Hydrogen Energy* **2024**, *68*, 491–498. [[CrossRef](#)]
45. Zhang, P.; Deng, X.; Li, W.; Ma, Z.; Wang, X. Electrochemical-induced surface reconstruction to NiFe-LDHs-based heterostructure as novel positive electrode for supercapacitors with enhanced performance in neutral electrolyte. *Chem. Eng. J.* **2022**, *449*, 137886. [[CrossRef](#)]
46. Zhang, J.; Lian, J.; Jiang, Q.; Wang, G. Boosting the OER/ORR/HER activity of Ru-doped Ni/Co oxides heterostructure. *Chem. Eng. J.* **2022**, *439*, 135634. [[CrossRef](#)]
47. Wang, Y.; Ma, J.; Wang, J.; Chen, S.; Wang, H.; Zhang, J. Interfacial Scaffolding Preparation of Hierarchical PBA-Based Derivative Electrocatalysts for Efficient Water Splitting. *Adv. Energy Mater.* **2019**, *9*, 1802939. [[CrossRef](#)]
48. Friebel, D.; Louie, M.W.; Bajdich, M.; Sanwald, K.E.; Cai, Y.; Wise, A.M.; Cheng, M.-J.; Sokaras, D.; Weng, T.C.; Alonso-Mori, R.; et al. Identification of Highly Active Fe Sites in (Ni,Fe)OOH for Electrocatalytic Water Splitting. *J. Am. Chem. Soc.* **2015**, *137*, 1305–1313. [[CrossRef](#)]
49. Corrigan, D.A. The Catalysis of the Oxygen Evolution Reaction by Iron Impurities in Thin Film Nickel Oxide Electrodes. *J. Electrochem. Soc.* **1987**, *134*, 377. [[CrossRef](#)]
50. Zhu, K.; Liu, H.; Li, M.; Li, X.; Wang, J.; Zhu, X.; Yang, W. Atomic-scale topochemical preparation of crystalline Fe³⁺-doped β-Ni(OH)₂ for an ultrahigh-rate oxygen evolution reaction. *J. Mater. Chem. A* **2017**, *5*, 7753–7758. [[CrossRef](#)]
51. Swierk, J.R.; Klaus, S.; Trotochaud, L.; Bell, A.T.; Tilley, T.D. Electrochemical Study of the Energetics of the Oxygen Evolution Reaction at Nickel Iron (Oxy)Hydroxide Catalysts. *J. Phys. Chem. C* **2015**, *119*, 19022–19029. [[CrossRef](#)]
52. Lu, Z.; Xu, W.; Zhu, W.; Yang, Q.; Lei, X.; Liu, J.; Li, Y.; Sun, X.; Duan, X. Three-dimensional NiFe layered double hydroxide film for high-efficiency oxygen evolution reaction. *Chem. Commun.* **2014**, *50*, 6479–6482. [[CrossRef](#)]
53. Song, F.; Hu, X. Exfoliation of layered double hydroxides for enhanced oxygen evolution catalysis. *Nat. Commun.* **2014**, *5*, 4477. [[CrossRef](#)]
54. Gao, X.; Long, X.; Yu, H.; Pan, X.; Yi, Z. Ni Nanoparticles Decorated NiFe Layered Double Hydroxide as Bifunctional Electrochemical Catalyst. *J. Electrochem. Soc.* **2017**, *164*, H307–H310. [[CrossRef](#)]
55. Zhu, X.; Tang, C.; Wang, H.F.; Zhang, Q.; Yang, C.; Wei, F. Dual-sized NiFe layered double hydroxides in situ grown on oxygen-decorated self-dispersal nanocarbon as enhanced water oxidation catalysts. *J. Mater. Chem. A* **2015**, *3*, 24540–24546. [[CrossRef](#)]
56. Batchellor, A.S.; Boettcher, S.W. Pulse-Electrodeposited Ni-Fe (Oxy)hydroxide Oxygen Evolution Electrocatalysts with High Geometric and Intrinsic Activities at Large Mass Loadings. *ACS Catal.* **2015**, *5*, 6680–6689. [[CrossRef](#)]
57. Yu, M.; Moon, G.; Bill, E.; Tueysuez, H. Optimizing Ni-Fe Oxide Electrocatalysts for Oxygen Evolution Reaction by Using Hard Templating as a Toolbox. *ACS Appl. Energy Mater.* **2019**, *2*, 1199–1209. [[CrossRef](#)]
58. Babar, P.T.; Lokhande, A.C.; Gang, M.G.; Pawar, B.S.; Pawar, S.M.; Kim, J.H. Thermally oxidized porous NiO as an efficient oxygen evolution reaction (OER) electrocatalyst for electrochemical water splitting application. *J. Ind. Eng. Chem.* **2018**, *60*, 493–497. [[CrossRef](#)]
59. Lin, Y.C.; Chuang, C.H.; Hsiao, L.Y.; Yeh, M.-H.; Ho, K.C. Oxygen Plasma Activation of Carbon Nanotubes-Interconnected Prussian Blue Analogue for Oxygen Evolution Reaction. *ACS Appl. Mater. Interfaces* **2020**, *12*, 42634–42643. [[CrossRef](#)]
60. Liang, H.; Meng, F.; Cabán-Acevedo, M.; Li, L.; Forticaux, A.; Xiu, L.; Wang, Z.; Jin, S. Hydrothermal Continuous Flow Synthesis and Exfoliation of NiCo Layered Double Hydroxide Nanosheets for Enhanced Oxygen Evolution Catalysis. *Nano Lett.* **2015**, *15*, 1421–1427. [[CrossRef](#)]
61. Zhang, H.; Li, X.; Hähnel, A.; Naumann, V.; Lin, C.; Azimi, S.; Schweizer, S.L.; Maijenburg, A.W.; Wehrspohn, R.B. Bifunctional Heterostructure Assembly of NiFe LDH Nanosheets on NiCoP Nanowires for Highly Efficient and Stable Overall Water Splitting. *Adv. Funct. Mater.* **2018**, *28*, 1706847. [[CrossRef](#)]
62. Wang, D.; Zhang, Y.; Fei, T.; Mao, C.; Song, Y.; Zhou, Y.; Dong, G. NiCoP/NF 1D/2D Biomimetic Architecture for Markedly Enhanced Overall Water Splitting. *ChemElectroChem* **2021**, *8*, 3064–3072. [[CrossRef](#)]
63. Pan, Y.; Sun, K.; Liu, S.; Cao, X.; Wu, K.; Cheong, W.C.; Chen, Z.; Wang, Y.; Li, Y.; Liu, Y.; et al. Core-Shell ZIF-8@ZIF-67-Derived CoP Nanoparticle-Embedded N-Doped Carbon Nanotube Hollow Polyhedron for Efficient Overall Water Splitting. *J. Am. Chem. Soc.* **2018**, *140*, 2610–2618. [[CrossRef](#)]
64. Gao, X.; Zhang, H.; Li, Q.; Yu, X.; Hong, Z.; Zhang, X.; Liang, C.; Lin, Z. Hierarchical NiCo₂O₄ Hollow Microcuboids as Bifunctional Electrocatalysts for Overall Water-Splitting. *Angew. Chem. Int. Ed.* **2016**, *55*, 6290–6294. [[CrossRef](#)] [[PubMed](#)]
65. Li, X.-P.; Zheng, L.R.; Liu, S.J.; Ouyang, T.; Ye, S.; Liu, Z.Q. Heterostructures of NiFe LDH hierarchically assembled on MoS₂ nanosheets as high-efficiency electrocatalysts for overall water splitting. *Chin. Chem. Lett.* **2022**, *33*, 4761–4765. [[CrossRef](#)]
66. Gong, Y.; Lin, Y.; Yang, Z.; Wang, J.; Pan, H.; Xu, Z.; Liu, Y. Crossed NiCo₂S₄ Nanowires Supported on Nickel Foam as a Bifunctional Catalyst for Efficient Overall Water Splitting. *ChemistrySelect* **2019**, *4*, 1180–1187. [[CrossRef](#)]
67. Han, G.-Q.; Li, X.; Liu, Y.R.; Dong, B.; Hu, W.-H.; Shang, X.; Zhao, X.; Chai, Y.M.; Liu, Y.Q.; Liu, C.G. Controllable synthesis of three dimensional electrodeposited Co-P nanosphere arrays as efficient electrocatalysts for overall water splitting. *RSC Adv.* **2016**, *6*, 52761–52771. [[CrossRef](#)]

68. Zhang, B.; Qiu, S.; Xing, Y.; Zhao, G.; Liao, W.; Mu, L.; Zhao, N. Introduction of Cationic Vacancies into NiFe LDH by In Situ Etching To Improve Overall Water Splitting Performance. *Langmuir* **2023**, *39*, 18152–18160. [[CrossRef](#)]
69. Liu, B.; Li, S.; Wang, T.; Yang, Y.; Wang, L.; Zhang, X.; Liu, Z.; Niu, L. Construction of CoFe bimetallic phosphide microflowers electrocatalyst for highly efficient overall water splitting. *Catal. Commun.* **2023**, *175*, 106607. [[CrossRef](#)]
70. Zai, S.F.; Zhou, Y.T.; Yang, C.C.; Jiang, Q. Al, Fe-Codoped CoP nanoparticles anchored on reduced graphene oxide as bifunctional catalysts to enhance overall water splitting. *Chem. Eng. J.* **2021**, *421*, 127856. [[CrossRef](#)]
71. Ji, D.; Peng, S.; Fan, L.; Li, L.; Qin, X.; Ramakrishna, S. Thin MoS₂ nanosheets grafted MOFs-derived porous Co-N-C flakes grown on electrospun carbon nanofibers as self-supported bifunctional catalysts for overall water splitting. *J. Mater. Chem. A* **2017**, *5*, 23898–23908. [[CrossRef](#)]
72. Guo, P.; Wu, R.; Fei, B.; Liu, J.; Liu, D.; Yan, X.; Pan, H. Multifunctional bayberry-like composites consisting of CoFe encapsulated by carbon nanotubes for overall water splitting and zinc-air batteries. *J. Mater. Chem. A* **2021**, *9*, 21741–21749. [[CrossRef](#)]
73. Maheskumar, V.; Saravanakumar, K.; Yea, Y.; Yoon, Y.; Park, C.M. Construction of heterostructure interface with FeNi₂S₄ and CoFe nanowires as an efficient bifunctional electrocatalyst for overall water splitting and urea electrolysis. *Int. J. Hydrogen Energy* **2023**, *48*, 5080–5094. [[CrossRef](#)]

Disclaimer/Publisher's Note: The statements, opinions and data contained in all publications are solely those of the individual author(s) and contributor(s) and not of MDPI and/or the editor(s). MDPI and/or the editor(s) disclaim responsibility for any injury to people or property resulting from any ideas, methods, instructions or products referred to in the content.